Computational Structural Engineering
An International Journal
Vol. 3, No. 1, pp. 19~29 (2003)

Computational Structural Engineering Institute

Buckling Analysis of Grid-Stiffened Composite Plates Using Hybrid Element with Drilling D.O.F.

Maenghyo Cho† and Won Bae Kim

†*School of Mechanical and Aerospace Engineering, Seoul National University, Seoul 151-742, Republic of Korea*
Department of Aerospace Engineering, Inha University, Inchon 402-751, Republic of Korea

Received November 2002; Accepted October 2003

ABSTRACT

In the present study, finite element linear buckling analysis is performed for grid-stiffened composite plates. A hybrid element with drilling degrees of freedom is employed to reduce the effect of the sensitivity of mesh distortion and to match the degrees of freedom between skins and stiffeners. The preliminary static stress distribution is analyzed for the determination of accurate load distribution. Parametric study of grid structures is performed and three types of buckling modes are observed. The maximum limit of buckling load was found at the local skin-buckling mode. In order to maximize buckling loads, stiffened panels need to be designed to be buckled in skin-buckling mode.

Keywords: buckling analysis, grid-stiffened plate, finite element analysis

1. Introduction

The weight reduction of structures is major concern for the high performance of aerospace vehicle. Grid-stiffened composite structures such as isogrid structures are promising advanced light-weight structures, which can substitute the metal grid structures and sandwich structures. Since grid-stiffened structures are made thin for the weight saving, they are weak under compressive loads. Thus buckling analyses are very important to decide structural design parameters. However, the buckling modes of the stiffened structures are quite complicated because both the skin and stiffeners are buckled simultaneously in the optimized configuration. The smeared macro-cell model which was used in the static analysis (Chen and Tsai, 1996) is not applicable to the buckling analysis.

The analytical approach by Rayleigh-Ritz energy method with Lagrange multiplier compatibility constraints was developed by Gürdal (Gürdal and Grall, 1994; Gürdal and Gendron, 1993; Phillips and Gürdal, 1990, 1992). However, for the problems with complex boundary geometry such as cutouts, finite element method is preferred. In the isogrid and cross-stiffened structures, compatibility condition at the interface between skin and stiffeners needs to be satisfied. To meet this condition, the drilling degrees of freedom need to be employed in the in-plane dimension of the skin. This drilling degrees of freedom of skin is matched with the bending rotational angles of the stiffeners. In the present study, two four-noded finite elements are developed for composite grid-stiffened plates. Both of them have drilling degrees of freedom. One is an isoparametric and the other is an assumed stress hybrid element. The motivation of the second one is to reduce the mesh sensitivity effect in the distorted mesh configurations.

The buckling analysis of the grid-stiffened structures requires a great amount of computer resource since they require a large number of meshes to describe local and global buckling modes. Especially for the weight optimization, repeated buckling analyses are required. Thus, efficient computation of buckling analysis plays a key role in the optimization program. Therefore, the present study aims at the development of an efficient linear finite element buckling analysis for the grid-stiffened structures.

2. Formulation

The four-noded hybrid shell element for isotropic mate-

† Corresponding author
Tel: +82-2-880-7322, Fax: +82-2-883-1513
E-mail address: mhcho@snu.ac.kr

rials developed by Aminpour (Aminpour, 1992; Rengarajan *et al.*, 1995) is the one with excellent performance in the linear analysis among the existing four-noded elements. In the present study, we extend this element to the buckling analysis of composite stiffened structures. First of all, in the element development, the drilling degree of freedom needs to be added in the nodal degrees of freedom, because the rotational degrees of freedom of stiffener are not matched with those of skin in the Mindlin plate model. Drilling degrees of freedom are defined as the rotational degrees of freedom normal to the plane of the element.

To compare the performance of Aminpours hybrid shell element with that of isoparametric element with drilling degrees of freedom, Allman-type shape functions are used (Allman, 1984; Cook *et al.*, 1986). This element has the same displacement field as that of Aminpours hybrid element.

In the linear buckling analyses, two types of loadings are considered. One is stress loading, and the other is displacement loading. The load distributions of grid-stiffened structures depend upon the skin thickness, stiffener thickness and height. The calculation of load distribution that should be performed before the buckling analysis is carried out. Thus in the present study, the two step buckling analysis is performed. The first step is to calculate stress distribution by static analysis, and the second step is to analyze linear buckling with the load distributions computed by the first step.

2.1 Assumed-Stress Hybrid Element Formulation

This hybrid element was originally developed by Aminpour and the formulation is simply outlined here. The detailed description and benchmark examples are given in Ref 8.

The present hybrid element formulation is based on Hellinger-Reissner variational principle. The Hellinger-Reissner functional can be written as

$$\Pi_{HR} = -\frac{1}{2}\int_V \{\sigma\}^T [S]\{\sigma\} dV + \int_V \{\sigma\}^T [L]\{u\} dV - \int_{S_\sigma} \{u\}^T \{t_o\} dS \tag{1}$$

where $[S]$ is the compliance matrix, and $[L]$ is the linear differential operator on the displacements $\{u\}$ to produce strains.

The stress and the displacement field are described as

$$\{\sigma\} = [P]\{\beta\} \tag{2}$$

$$\{u\} = [N]\{q\} \tag{3}$$

where $[P]$ and $[N]$ are matrices of stress and displacement interpolation functions, and $\{\beta\}$ and $\{q\}$ are the unknown stress parameter and nodal displacement vectors,respectively.

Imposing stationary conditions on the functional Π_{HR}, finally we can get the following equations.

$$\{\beta\} = [H]^{-1}[T]\{q\} \tag{4}$$

$$[K] = [T]^T[H]^{-1}[T] \tag{5}$$

$$[K]\{q\} = \{F\} \tag{6}$$

where

$$[H] = \int_V [P]^T[S][P] dV \tag{7}$$

$$[T] = \int_V [P]^T[L][N] dV \tag{8}$$

$$\{F\} = \int_{S_\sigma} [N]^T\{t_o\} dS \tag{9}$$

where V, S_σ and $\{t_o\}$ are the volume of the plate, stress prescribed boundary and traction vector given along the boundary. By solving linear stiffness equations given in Eqn(6), the conventional nodal displacement vectors can be obtained.

2.2 Assumed-Stress Field

The membrane part of assumed-stress field can be expressed in the natural coordinate system.

$$\begin{aligned} N_\xi &= \beta_1 + \beta_4\xi + \beta_6\eta + \beta_8\eta^2 \\ N_\eta &= \beta_2 + \beta_5\xi + \beta_7\eta + \beta_9\xi^2 \\ N_{\xi\eta} &= \beta_3 - \beta_4\eta - \beta_7\xi \end{aligned} \tag{10}$$

The bending part of assumed-stress field is also given in the natural coordinates(i.e. $\xi-\eta$ coordinates) as follows

$$\begin{aligned} M_\xi &= \bar{\beta}_1 + \bar{\beta}_4\xi + \bar{\beta}_6\eta + \bar{\beta}_8\eta^2 \\ M_\eta &= \bar{\beta}_2 + \bar{\beta}_5\xi + \bar{\beta}_7\eta + \bar{\beta}_9\eta^2 \\ M_{\xi\eta} &= \bar{\beta}_3 + \bar{\beta}_{10}\xi + \bar{\beta}_{11}\eta + \frac{1}{2}\bar{\beta}_{12}\xi^2 + \frac{1}{2}\bar{\beta}_{13}\eta^2 \end{aligned} \tag{11}$$

The shear resultant fields are given by satisfying plate equilibrium equations.

$$Q_\xi = \bar{\beta}_4 + \bar{\beta}_{11} + \bar{\beta}_{13}\eta$$
$$Q_n = \bar{\beta}_7 + \bar{\beta}_{10} + \bar{\beta}_{12}\xi \tag{12}$$

2.3 Displacement Field

To handle drilling degrees of freedom, the Allman-type shape functions are used. The in-plane field has quadratic displacement functions considering the difference of drilling rotations.

$$u^\circ(\xi,\eta) = \sum_{i=1}^{4} N_i u_i + \sum_{i=1}^{4} \frac{\Delta y_i}{8} N_i^*(\theta_{zj} - \theta_{zi})$$
$$u^\circ(\xi,\eta) = \sum_{i=1}^{4} N_i \upsilon_i - \sum_{i=1}^{4} \frac{\Delta x_i}{8} N_i^*(\theta_{zj} - \theta_{zi}) \tag{13}$$

where

$\Delta x_i = x_j - x_i$, $\Delta y_i = y_j - y_i$

$$N_i = \frac{1}{4}(1+\xi_i\xi)(1+\eta_i\eta), \quad i = 1,2,3,4 \tag{14}$$

$$N_i^* = \begin{cases} \frac{1}{2}(1-\xi^2)(1+\eta_i\eta), & i = 1,3 \\ \frac{1}{2}(1-\eta^2)(1+\xi_i\xi), & i = 2,4 \end{cases} \tag{15}$$

and

$$j = \begin{cases} i+1, & i = 1,2,3 \\ 1, & i = 4 \end{cases}$$

The out-of-plane displacement field is given by

$$w^\circ(\xi,\eta) = \sum_{i=1}^{4} N_i w_i - \sum_{i=1}^{4} \frac{\Delta y_i}{8} N_i^*(\theta_{xj} - \theta_{xi}) + \sum_{i=1}^{4} \frac{\Delta x_i}{8} N_i^*(\theta_{yj} - \theta_{yi})$$
$$\theta_x(\xi,\eta) = \sum_{i=1}^{4} N_i \theta_{xi}$$
$$\theta_y(\xi,\eta) = \sum_{i=1}^{4} N_i \theta_{yi} \tag{16}$$

where θ_x, θ_y are rotational field and θ_{xi}, θ_{yi}, θ_{zi} are the nodal rotational displacements. Using Eqns (10), (11). and (12) for stress fields and Eqns (13) and (16) for displacement fields, the final element equation can be obtained in the form of Eqn(6).

2.4 Geometric Stiffness Matrix

The geometric stiffness matrix is derived by using the full non-linear Green-Lagrange strain tensor.

$$e_{ij} = \frac{1}{2}\left(\frac{\partial u_i}{\partial x_j} + \frac{\partial u_j}{\partial x_i} + \frac{\partial u_k}{\partial x_i}\frac{\partial u_k}{\partial x_j}\right) \tag{17}$$

Using Mindlin kinematic assumptions, strains can be expressed by two parts such as membrane and bending strains.

$$\{e\} = \{e^o\} + z\{k\} \tag{18}$$

The membrane strains can be written as Eqn(19).

$$\{e^o\} = \{e_L^o\} + \{e_{NL}^o\} \tag{19}$$

where e_{NL}^o is a nonliear strain part. The generalized Hellinger-Reissner functional including the non-linear strains can be written as Eqn(20).

$$II_{HR} = -\frac{1}{2}\int_V \{\sigma\}^T[S]\{\sigma\}dV + \int_V \{\sigma\}^T[L]\{u\}dV - \int_V \{\sigma_o\}^T[e_{NL}^o]dV - \int_{S_\sigma} \{u\}^T\{t_o\}ds \tag{20}$$

where $\{\sigma_o\}$ is the prescribed prebuckling stress state. Upon substitution of the displacement and stress approximations, Hellinger-Reissner functional reduces to Eqn(21).

$$II_{HR} = -\frac{1}{2}\{\beta\}^T[H]\{\beta\} + \{\beta\}^T[T]\{q\} - \{q\}^T\{F\} + \frac{1}{2}\{q\}^T[K_\sigma]\{q\} \tag{21}$$

The geomatric stiffness matrix $[K_\sigma]$ is given by Eqn(22).

$$[K_\sigma] = \int_A [N]^T[G]^T[Y][G][N]dA \tag{22}$$

where A means the integral domain

The matrix [G] and [Y] is written as Egn(23) and Egn(24).

$$|G| = \begin{bmatrix} \partial_x & 0 & 0 & 0 & 0 & 0 \\ \partial_y & 0 & 0 & 0 & 0 & 0 \\ 0 & \partial_x & 0 & 0 & 0 & 0 \\ 0 & \partial_y & 0 & 0 & 0 & 0 \\ 0 & 0 & \partial_x & 0 & 0 & 0 \\ 0 & 0 & \partial_y & 0 & 0 & 0 \end{bmatrix} \tag{23}$$

$$[Y] = \begin{bmatrix} S & 0 & 0 \\ 0 & S & 0 \\ 0 & 0 & S \end{bmatrix} \tag{24}$$

where S is the matrix of prebuckling stress state.

$$S = \begin{bmatrix} N_x^o & N_{xy}^o \\ N_{xy}^o & N_y^o \end{bmatrix} \tag{25}$$

where the superscript ° means the prebuckling state. Using the stiffness matrix in Eqn(5) and the geometric stiffness matrix in Eqn(22), we can solve the eigenvalue problem of linear buckling.

3. Numerical Examples

In this section, two categories of examples are shown. The examples of one category are to assess the performance of hybrid element in the mesh distortion, and the other is the parametric study for the grid structures. To evaluate the developed hybrid element performance in the grid-stiffened composite structures, the examples of buckling analyses of cross-ply composite rectangular plate and 1-cell/3-cell cross-stiffened panel are considered. In order to investigate the effect of stiffener size in grid structures, the parametric studies of cross-stiffened structures and isogrid structures are presented. The buckling analysis of cross-ply composite rectangular plate in the first example is performed under the stress loading, and the analyses of grid structures are performed under the displacement loading.

In the following examples, the isoparametric element indicates the displacement-based element with drilling degrees of freedom and hybrid element indicates the Aminpour's hybrid element. For the convenience of comparisons, only eigen problem routine by inverse power method is considered in calculating solving time, and it is normalized with respect to that of the minimum mesh configuration at each examples. The examples of one category are for the assessment and the examples of the other are for parametric study.

3.1 Composite Rectangular Plate

This example shows the performance of the proposed hybrid element both in the uniform meshes and in the distorted mesh configurations. In the cross-stiffened and isogrid plates and shells, stiffeners are attached to the skin with the inclined angles. To satisfy the displacement compatibility between stiffeners and skin plates, the distorted mesh configuration cannot be avoided. Therefore, the performance of the plate buckling in the distorted mesh configuration is critical.

Regular mesh configuration is shown in Figures 1(a) and 1(b). Figure 1(a) shows 8×8 mesh, and 16×16 mesh configurations are shown in Figure 1(b). The number of elements in Figures 1(a) and 1(b) are 64 and 256, and each of them has 486 and 1734 degrees of freedom, respectively. Figures 1(c) and 1(d) show the distorted mesh configuration. Figure 1(c) has 48 elements with 342 D.O.F.s', and Figure 1(d) has 192 elements with 1254 D.O.F.s' The side length of square plate is 10 inch and thickness is 0.1 inch. The material properties are given in Table 1. The plate is a cross-ply composite laminate with $[0/90/0/90]_s$ layups and all edges are simply-supported. The numerical results of regular mesh and distorted mesh are in Tables 2 and 3. Nondimensionalized critical buckling loads are defined as

$$\bar{N} = N_{cr}\frac{a^2}{E_2 h^3} \tag{26}$$

Where N_{cr}, a, and h are the critical buckling load, in-plane characteristic length and thickness of the plate. E_2 is the elastic modulus in the direction perpendicular to the fiber alignment. The exact solution is given in the Ref 11. As shown in Table 2, the values of buckling loads of both elements converge rapidly. The results of the hybrid element converge more rapidly than those of the isoparametric element with drilling D.O.F., but the advantage of the rate of convergence of the former over the latter is mar-

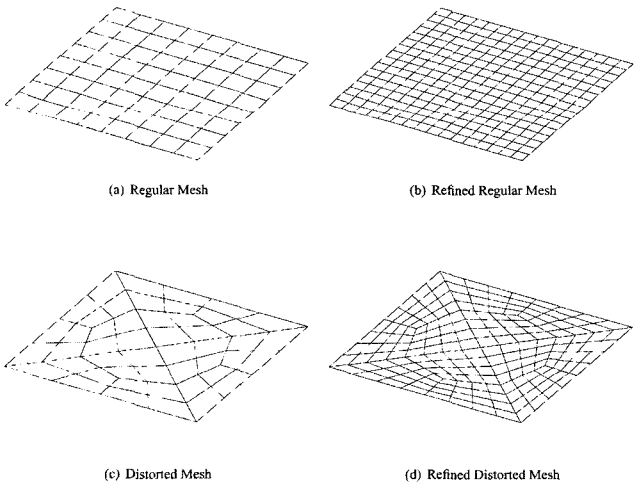

Fig. 1. Mesh Configuration of Rectangular Plate

Table 1. Lamina Properties in Cross-Ply Laminates

Longitudinal Modulus $E_1 = 10.0 \times 10^6$ *lbf=in*^{2}
Transverse Modulus $E_2 = 0.1 \times E^1$
In-Plane Shear Modulus $G_{12} = 0.5 \times E^2$
Transverse Shear Modulus $G_{23} = 0.2 \times E^2$
In-Plane Poisson's Ratio $v_{12} = 0.25$

ginal. However, as shown in Table 3, the accurate buckling predictions are provided by the hybrid element even in the distorted coarse meshes(12 element case), which cannot be expected in the isoparametric element.

3.2 1-Cell/3-Cell Cross-Stiffened Plate

Before analyzing multi-cell plates, only one-cell stiffened plate with cross-stiffener was analyzed with both the isoparametric element with drilling D.O.F. and the hybrid element. The geometric configuration is shown in Figure 2. It has 112 elements and 750 degrees of freedom.

The each side lengths of skin part(both x and y directions) are 28 inch, and the thickness is 0.2 inch. A quasi-isotropic layups are considered and the stacking sequence is $[\pm 45/0/90]_S$. The thickness of stiffener is 0.2 inch with 8-ply of 0 degree, and the height is 0.5 inch. The material

Table 2. Buckling Loads for Regular Mesh Configuration

# of Element	16	64	256	1024
# of D.O.F.	150	486	1734	6534
Solving Time	1	8	97	1312
Iso-Parametric Element	11.89	11.26	11.16	11.13
Hybrid Element	10.92	11.07	11.10	11.11
Exact		10.83		

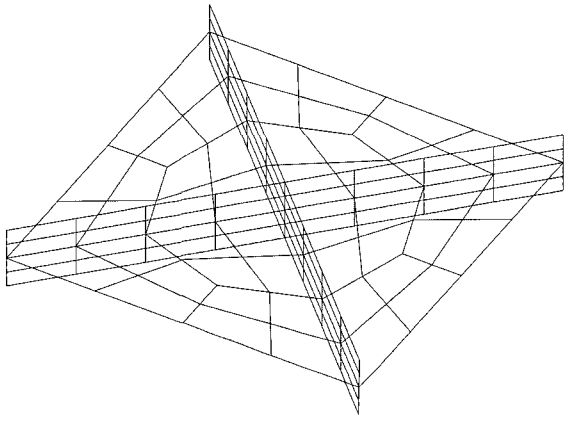

Fig. 2. Mesh Configuration of 1-Cell Cross-Stiffened Plate

Table 3. Buckling Loads for Distorted Mesh Configuration

# of Element	12	48	192	768
# of D.O.F.	102	342	1254	4806
Solving Time	1	9	117	1631
Iso-Parametric Element	28.56	11.75	11.22	11.14
Hybrid Element	10.92	11.11	11.10	11.10
Exact		10.83		

properties are given in Table 4. All the boundaries are simply-supported and the buckling results are given in Table 5.

The convergent buckling load is around 970~980 *lbf/in* according to the analysis of the very refined meshes (11,046 D.O.F.). With smaller solving time, the hybrid element provides very accurate buckling load within 1% error. Even in the very coarse meshes with about 100 elements, the relative error by the hybrid method is only within 3%. However, the isoparametric element provides poor prediction of buckling load, in which the relative error is up to 17%. The accuracy of errors within 3% and the efficiency of solving time less than 2 seconds should be emphasized. For example, in a problem of structural optimization considering buckling that requires repeated computations, solving time can be reduced tremendously.

The buckling of 3-cell cross-stiffened plate was analyzed. They can be considered as the component of aircraft wing or fuselage. The material properties are same as those in the case of one-cell and the geometric dimensions are 28 inch and 80 inch. Uniaxial compression is applied along the 80-inch edge. The mesh configuration is shown

Table 4. Lamina Properties in Cross-Stiffened Plate

Longitudinal Modulus $E_1 = 18.5 \times 10^6$ *lbf/in*^{2}
Transverse Modulus $E_2 = 1.64 \times 10^6$ *lbf/in*^{2}
In-Plane Shear Modulus $G_{12} = 0.87 \times 10^6$ *lbf/in*^{2}
Transverse Shear Modulus $G_{23} = 0.54 \times 10^6$ *lbf/in*^{2}
In-Plane Poissons Ratio $v_{12} = 0.30$

Table 5. Buckling Loads of 1-Cell Cross-Stiffened Plate

# of Element	112	448	1792
# of D.O.F.	750	2838	11046
Solving Time	1	12	79
Iso-Parametric Element	1133.1	1002.6	969.7
Hybrid Element	1003.6	972.8	975.9

(*lbf/in*)

in Figure 3. All the boundaries are simply-supported and the results of the buckling analysis are given in Table 6.

While the convergence of isoparametric element is quite slow, the hybrid element shows much faster convergence. The accuracy of more than 30,000 D.O.F.s' by the isoparametric element with almost one hour computation time can be achieved by only 8,000 D.O.F.s' hybrid element within five minutes. The computational efficiency is greater as the number of the repeated grid increases.

3.3 Parametric Studies of Cross-Stiffened Plate

In the design of grid structures, there are many design parameters such as skin thickness, skin and stiffener layups, stiffener thickness and height, grid type, number of grid, and so on. This example shows how buckling loads and modes of cross-stiffened plates change as the number of grid and the height of stiffeners change. The 2-cell, 3-cell, and 4-cell cross-stiffened plates are considered. To apply same weight condition, cross-sectional area of stiffener is kept constant (0.01 in^2).

The buckling loads vs. the height of stiffener are shown in Figure 4. Stiffener height varies from 0.4 *in* to 1.0 *in* in each case.

There are three types of buckling modes in grid-stiffened structures. The first one is a global-buckling mode as shown in Figure 5(a). In this case, the role of stiffener is to add bending rigidity to skin. Therefore, within the global buckling mode range, the buckling loads increase as the height of the stiffeners increase.

The second is a local skin-buckling mode. Stiffeners do not show in-plane bending behavior(see Figure 8(a)) since this behavior requires large deformation energy. Instead, they tend to show out-ofplane bending behavior(see Figure 8(b)). However, in spite of out-of-plane bending behavior of the stiffeners, the deformation energy of this mode of stiffener is very small compared to that of skin in the skin-buckling mode (See Figure 6(d)).

The third mode is stiffener-buckling mode. This mode is observed when the load ratio of stiffener to the skin is relatively high and the thickness of the stiffeners are relatively small. In this case, skin has no out-of-plane deformation and only stiffeners are buckled. This mode is not observed in the present analysis of the practical range of application of the stiffener height.

The buckling loads of 2-cell cross-stiffened structures increase as the height grows. As shown in Figure 5(c), mode transition from global to skin-buckling occurs. From the buckling modes of the Figures 6 and 7, and buckling loads in Figure 4, it is observed that buckling loads of 3-cell and 4-cell crossstiffened plates in the range of 0.4~ 1.0 *in* depend on the types of buckling modes. In the case of 0.4 *in* height, the buckling mode shape is the mixed one between global-buckling and skin-buckling mode. As the stiffener height becomes higher than 0.6 *in*, the buckling modes and loads do not have significant changes. If the stiffener height is larger than 1 *in*, then the buckling mode shapes and buckling loads are almost the same.

From the parametric study, it is observed that there is a critical height of the stiffener in which the buckling mode

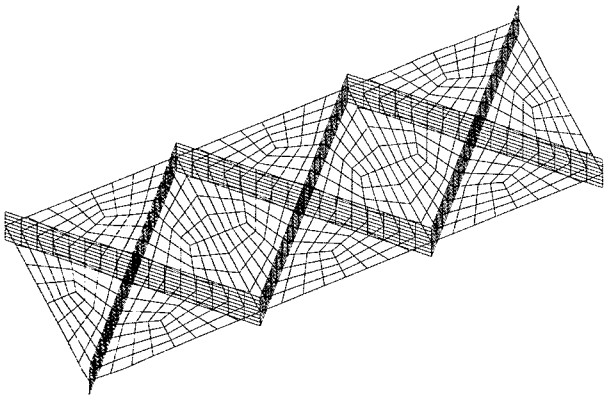

Fig. 3. Mesh Configuration of 3-Cell Cross-Stiffened Plate

Table 6. Buckling Loads of 3-Cell Cross-Stiffened Plate

# of Element	336	1344	5376
# of D.O.F.	2094	8214	32550
Solving Time	1	12	172
Iso-Parametric Element	926.0	669.4	640.9
Hybrid Element	693.6	646.6	636.5

(*lbf/in*)

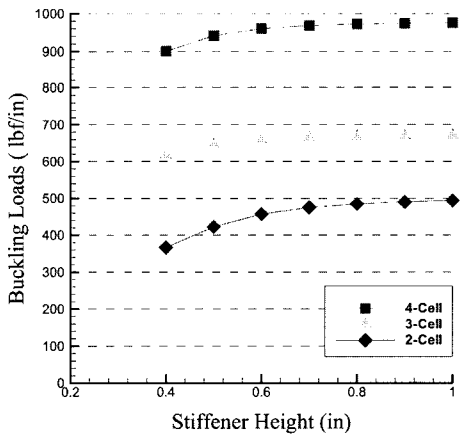

Fig. 4. Buckling Loads of Cross-Stiffened Panel

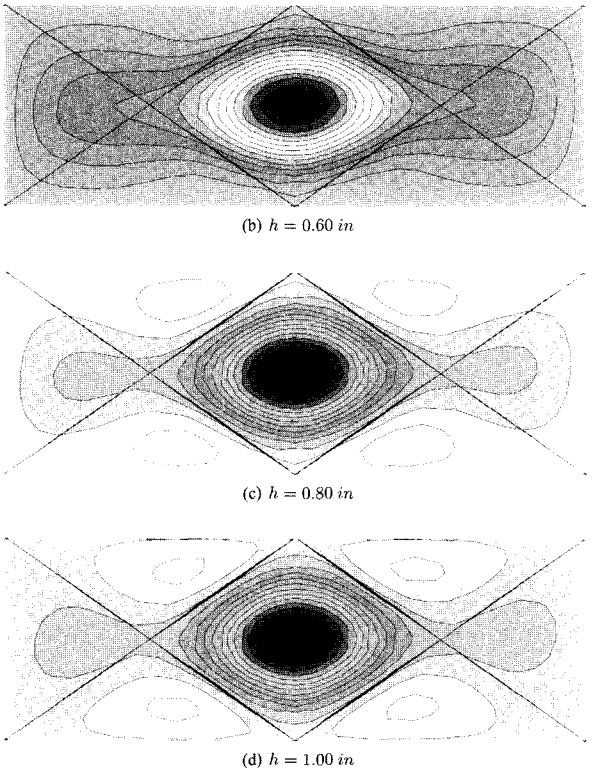

Fig. 5. Buckling Modes of 2-Cell Cross-Stiffened Plate

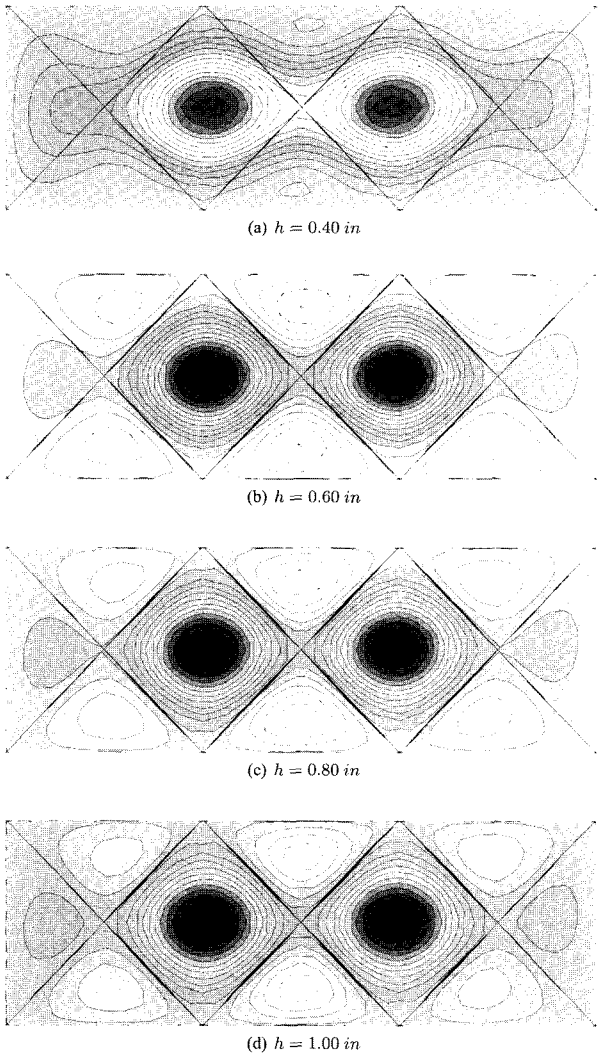

Fig. 6. Buckling Modes of 3-Cell Cross-Stiffened Plate

transition occurs. Once the mode change occurs from global to local skin buckling mode, the buckling load becomes almost the maximum critical value. The buckling load does not change significantly even though the stiffener height becomes larger than critical height.

3.4 Parametric Studies of Isogrid Plates

In the present analysis, the stiffeners are located only on the upper skin. This isogrid construction is applicable when smooth surface is required such as fuselage and wing skin of aircraft structures. In the present study, the geometry of skin is 21.5 *in* long and 18.6 *in* wide, 0.07 *in* thick, and $[(\pm 60/0)_4]$ layups. Only $[(0)_n]$ plies are arranged in the stiffener layups. The material properties are shown in Table 7. Displacement loading is applied on the long side edge in the parametric study. Boundary conditions are given in Figure 9. In the horizontal edges, the translational displacements u,w, and drilling degrees of freedom θ_z are fixed for both skin and stiffeners. In the vertical edges, displacements u and w are fixed in skin and stiffeners, but drilling degrees of freedom μz are constrained on the skin only.

In the parametric study of isogrid structure, two types of grid configuration are considered. One is a large-cell isogrid, and the other is smaller-cell isogrid case. In each case, mesh configurations are shown in Figures 12(a) and 13(a).

Table 7. Lamina Properties in Isogrid Pane

Longitudinal Modulus	$E_1 = 25.1 \times 10^6\ lbf/in^2$
Transverse Modulus	$E_2 = 1.1 \times 10^6\ lbf/in^2$
In-Plane Shear Modulus	$G_{12} = 0.8 \times 10^6\ lbf/in^2$
In-Plane Poissons Ratio	$\nu_{12} = 0.33$

Buckling modes of large-cell isogrid panel are shown in Figure 12. For the parametric study of large-cell isogrid panel, coarse mesh with 240 elements and 1482 degrees of freedom is used.

As shown in Figure 10, all three types of buckling modes appear as the stiffener height varies. In the smaller

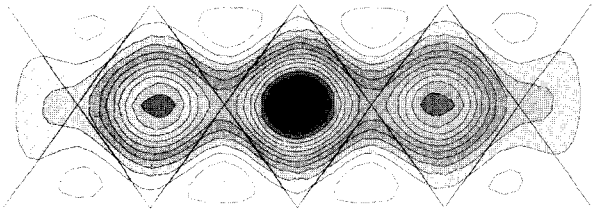

(a) $h = 0.40\ in$

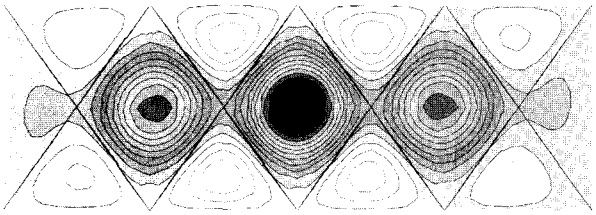

(b) $h = 0.60\ in$

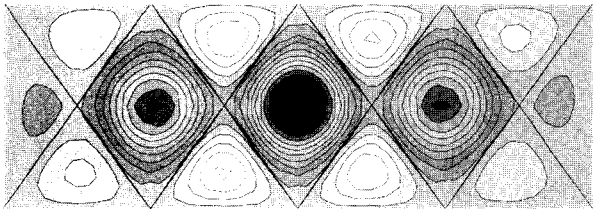

(c) $h = 0.80\ in$

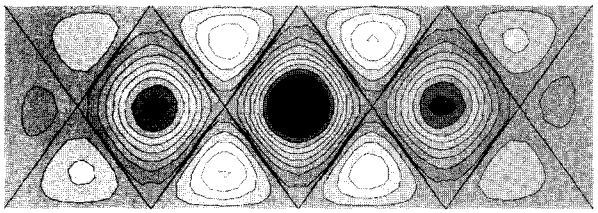

(d) $h = 1.00\ in$

Fig. 7. Buckling Modes of 4-Cell Cross-Stiffened Plate

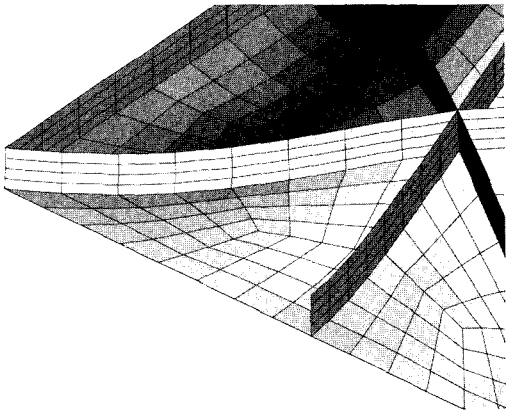

(a) In-Plane Stiffener Bending

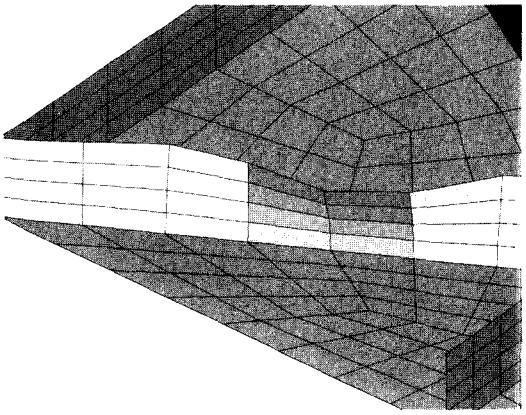

(b) Out-of-Plane Stiffener Bending

Fig. 8. In-Plane and Out-of-Plane Bending Deformation of Stiffener

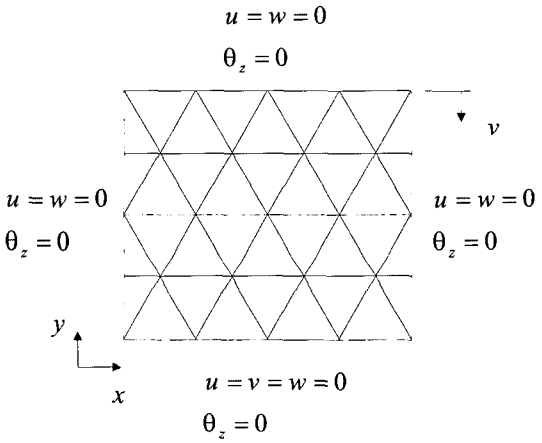

Fig. 9. Configuration of Isogrid Plate

height of stiffener ($0.1\ in \leq$ stiffener height $\leq 0.3\ in$), the global buckling mode appears, which is also shown in Figure 12(b). As discussed in the cross-stiffened plate case, the buckling loads are getting higher as the bending rigidity of stiffener becomes larger.

The stiffener height equal to about $0.3\ in$, the mode transition from the global to local skin buckling occurs and the buckling loads become constant and reaches the maximum. The role of stiffener is to give constraint to generate local higher buckling mode as shown in Figure 12(c).

If the stiffener height is larger than a certain critical value, then stiffener buckling occurs and the buckling loads rapidly decrease, which is depicted in Figure 10. In this buckling mode, there is no deformation energy stored in the skin plate. The mode shape is given in Figure 12(d).

From the parametric study, it is observed that as the cross-sectional area of stiffener is getting larger, the local skin buckling zone become wider. Thus we have more flexibility in the selection of stiffener height for the structural design when the relatively large cross-sectional area

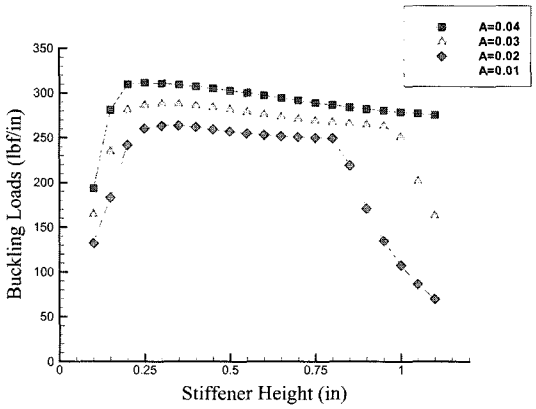

Fig. 10. Buckling Loads of Isogrid Panel

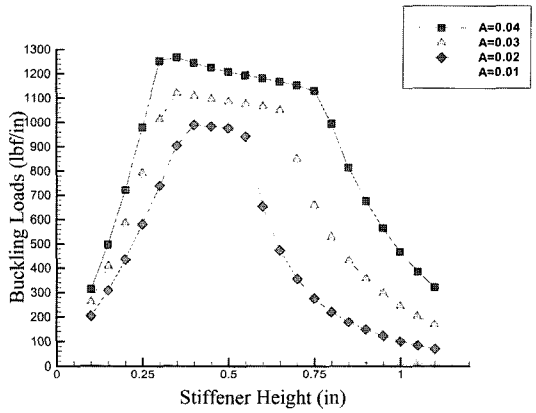

Fig. 11. Buckling Loads of Isogrid Panel

of isogrid stiffeners are considered.

If there are no stiffeners, the buckling load of skin is 20.2 *lbf/in* and the volume is 28.02 in^3. In the case of rib area is given as $A_{rib} = 0.01$ in^2, the volume of stiffener is 1.505 in^3 and is about 5% of that of skin. But the buckling loads are as large as 10 times of the case that there is only skin.

In the analyses of smaller-cell isogrid structures, refined mesh configuration required 3456 elements and 20478 degrees of freedom as shown in Figure 13(a). The coarse mesh configuration of this structure has only 864 elements and 5058 D.O.F.'s, and buckling mode and buckling loads are within 3% difference from those of the refined mesh case. To save computing time, coarse mesh configuration has been used in small-cell isogrid analysis. Its skin geometry is the same as large-cell and the difference between these two types of structures is only the number of grid.

Numerical results of the analysis of the smaller-cell case are in Figure 11. The qualitative buckling behavior of this case is similar to the case of larger-cell isogrid (see Figure 13(b)~13(d)), but the buckling loads are much larger compared to the case of large-cell. This is because the local skin-buckling mode of smaller-cell needs more bubbles (higher mode) than that of large-cell. In the smaller cross-sectional area of stiffener(A_{rib} = 0.01), no local skin buckling modes are observed. Thus maximum buckling loads occur at the transition from the global mode to the stiff-

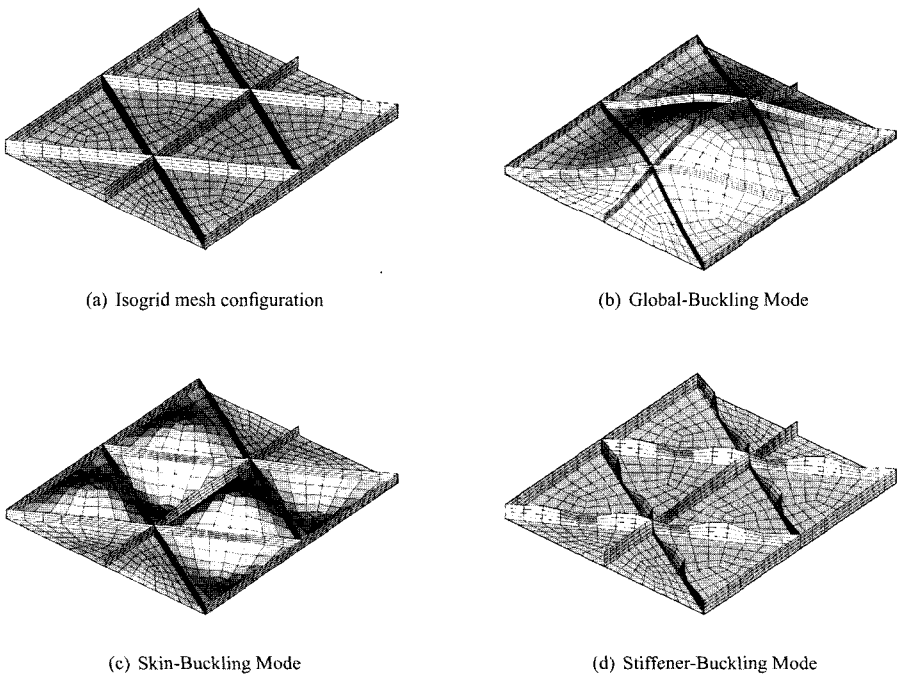

(a) Isogrid mesh configuration (b) Global-Buckling Mode

(c) Skin-Buckling Mode (d) Stiffener-Buckling Mode

Fig. 12. Mesh Configuration and Buckling Modes of Isogrid Panel

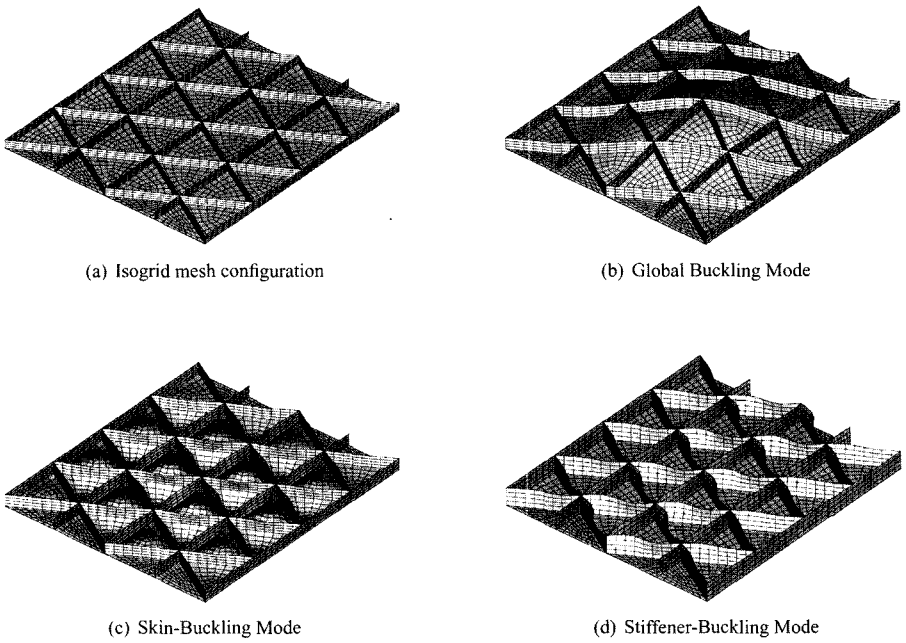

(a) Isogrid mesh configuration

(b) Global Buckling Mode

(c) Skin-Buckling Mode

(d) Stiffener-Buckling Mode

Fig. 13. Mesh Configuration and Buckling Modes of Isogrid Panel

ener-buckling modes. As the cross-sectional area increases, the local skin-buckling mode is observed in the zone of the intermediate stiffener height. The range of this mode is getting wider as the cross-sectional area becomes larger.

4. Conclusion

In the present study, an efficient linear buckling analysis of composite grid-stiffened plates has been performed. The employed four-noded hybrid element with drilling degrees of freedom demonstrated its accuracy and the efficiency.

The parametric study of cross-grid-stiffened and isogrid stiffened plate buckling analysis is performed. The following specific observations are made from this study.

1. There exist three types of buckling modes, that is, global mode, local skin-buckling mode, and stiffener-buckling mode.
2. In the practical range of application of stiffener heights, the global modes and local skin-buckling mode appear in the cross-grid stiffened plate. Whereas in the isogrid stiffened plate, all these modes appear.
3. Mode transition appears as the stiffener height increase from global-buckling to local skin-buckling or from local skin-buckling to stiffener-buckling.
4. Maximum buckling load occurs at the local skin-buckling mode. The range of skin-buckling is getting wider as the cross-sectional area of the grid-stiffener become larger.

To understand actual load-carrying capacity of the grid-stiffened panel, the postbuckling analysis is necessary. This work is now in progress.

References

Allman DJ (1984) A Compatible Triangular Element Including Vertex Rotations for Plane Elasticity Analysis,Comput. Struct., 19:1-8.

Aminpour MA (1992) An Assemed-stress Hybrid 4-node Shell Element with Drilling Degrees of Freedom, Int. J. for Numerical Methods in Eng., 33:19-38.

Aminpour MA (1992) Direct Formulation of a Hybrid 4-node Shell Element with Drilling Degrees of Freedom,Int. J. for Numerical Methods in Eng., 35:997-1013.

Chen HJ, Tsai SW (1996) Analysis and Optimum Design of Composite Grid Structures,Journal of Composite Materials,30(4):503-534.

Cook RD, Malkus DS, Plesha ME (1986) On the Allman triangle and a related quadrilateral element, Comput. Struct., 22:1065-1067.

Gürdal Z, Gendron G (1993) Optimal Design of Geodesically Stiffened Composite Cylindrical Shells, Composites Engineering, 3(12): 1131-1147.

Gürdal Z, Grall B (1994) Buckling Analysis of Geodesically Stiffened Composite Panels with Discrete Stiffeners, Jounal of Aircraft,31(5):1197-1204.

Phillips JL, Gürdal Z (1990) Structural Analysis and Optimum Design of Geodesically Stiffened Composite Panels, CCMS-90-05, Virginia Polytechnic Institute and State University, Blacksburg,

VA.

Phillips JL, Gürdal Z (1992) Optimum Design of Geodesically Stiffened Composite Cylindrical Shells, CCMS-92-93, Virginia Polytechnic Institute and State University, Blacksburg, VA.

Rengarajan G, Aminpour MA, Knight MF Jr (1995) Improved Assumed-Stress Hybrid Shell Element with Drilling Degrees of Freedom for Linear Stress, Buckling and Free Vibration Analyses, Int. J. for Numerical Methods in Eng., 38:1917-1943.

Reddy JN (1996) Mechanics of Laminated Composite Plates, CRC Press.